Journal of Materials Chemistry A

ROYAL SOCIETY OF CHEMISTRY

PAPER

View Article Online
View Journal | View Issue

Cite this: J. Mater. Chem. A, 2023, 11, 7526

Tailoring the electrocatalytic activity of multicomponent $(Co,Fe,Ni)_9S_{8-x}Se_x$ pentlandite solid electrodes†

Andrzej Mikuła, *[a] Maciej Kubowicz,[a] Julia Mazurków,[a] Krzysztof Mars,[a] Mathias Smialkowski,[b] Ulf-Peter Apfel[bc] and Marta Radecka[a]

The multi-component approach to materials design is gaining increasing popularity in energy-conversion-oriented applications. This study describes a 5-component multimetallic chalcogenide compound with a pentlandite structure that recently became increasingly interesting in terms of electrocatalytic water splitting. The solubility limit of Se in the trimetallic $Co_3Fe_3Ni_3S_8$ system was determined along with the potential effect of this additive on the material's intrinsic properties. This was followed by an unprecedented approach, an attempt to fabricate solid electrodes using the inductive hot-pressing method. The effects of the consolidation conditions on the morphology and final properties of the material are discussed in detail. Tailoring both the chemical composition and processing conditions (initial grain size, sintering temperature) can lead to the optimization of highly efficient electrocatalysts for water splitting. The best electrodes were characterized at elevated current densities of 120 mA cm^{-2}, showing low overpotentials (240 mV *versus* RHE) but with rather low electrochemical active surface area and moderately optimal reaction kinetics. It was therefore shown that using multi-component compositions resulted in good intrinsic properties of the materials toward hydrogen production, together with high density and vacancy concentrations provided by the sintering process, thus producing an efficient electrocatalyst using a simple, scalable method without any additional processing.

Received 14th November 2022
Accepted 1st March 2023

DOI: 10.1039/d2ta08893b

rsc.li/materials-a

Introduction

Considering the actual trends aimed at reducing the utilization of fossil fuels as a source of hydrogen and the growing popularity of energy-conversion processes (*e.g.* fuel cell technologies), electrocatalytic water splitting has become one of the most promising processes for environmentally friendly hydrogen production. State-of-the-art materials in this regard are mainly represented by Pt and other precious-metal-based compounds (the so-called platinum group metals, PGMs),[1–3] whose high cost and limited availability have led to an intensive search for new solutions. One of the most important criteria for designing potential alternatives to PGMs is the strength of the catalyst–H and catalyst–OH binding energies for the hydrogen (HER) and oxygen (OER) evolution reaction, respectively, and the related electronic structural properties.[1,2,4] These features indicate the enormous potential for transition metal (TM) compounds, including oxides and chalcogenides (Chs). The latter group offers a wide variety of chemical compositions as well as structures and is particularly interesting in this regard owing to the presence of edge and surface defect sites, tailorable morphologies, tunable electronic structures, and high electroconductivities.[5,6] For instance, TM disulfides, represented by different types of nanostructured cobalt, iron, and molybdenum disulfides (sometimes modified/doped by one of the other first-row 3d TMs), exhibit decent performances in various media, characterized by current densities of 10 mA cm^{-2} at low overpotentials (*e.g.* 96 mV for mesoporous FeS_2 (ref. 7) or 180 mV for Co-doped MoS_2 nanosheets[9]), *versus* the reference hydrogen electrode (RHE) and fast H_2 evolution ratio determined by low values of the Tafel slopes.[7,9–11] Outside of the $TMCh_2$ structures, other stoichiometries have also been considered for the HER catalysis, such as chalcopyrite $CuFeS_2$ or nickel sulfides (NiS, Ni_3S_2) showing good properties reaching current densities of 10 mA cm^{-2} at an overpotential of 330–450 mV, particularly after anchoring to graphene or gold surfaces.[2,12] Recently, metal chalcogenides have also attracted a lot of interest for their OER activity, potentially granting them the ability to operate as bi-functional (HER–OER) catalysts. For instance, Chen *et al.* have shown an overpotential of about 300 mV at a current density of 10 mA cm^{-2} and a Tafel slope of 47 mV dec^{-1} for NiS [8] towards

[a]AGH University of Science and Technology, Faculty of Materials Science and Ceramics, Al. Mickiewicza 30, 30-059 Krakow, Poland. E-mail: amikula@agh.edu.pl
[b]Ruhr-Universität Bochum, Fakultät für Chemie und Biochemie, Anorganische Chemie I, Universitätsstrasse 150, 44801 Bochum, Germany
[c]Fraunhofer UMSICHT, Department for Electrosynthesis, Osterfelder Str. 3, 46047 Oberhausen, Germany

† Electronic supplementary information (ESI) available. See DOI: https://doi.org/10.1039/d2ta08893b

both the HER and OER. Numerous studies have also shown that TMChs can be easily modified by doping processes,[9,13,14] shape engineering, and creating heterostructure or composite systems,[1,15,16] granting them improved catalytical performance.

However, despite the satisfactory electrochemical activity, the significantly lower electrical conductivities of transition metal chalcogenides when compared with noble metal-based catalysts often impose the need for additional surface engineering, involving the nanostructuring of actual catalysts (providing high surface expansion and defect concentration) and anchoring them to a highly conductive backbone (providing fast charge transfer).[2,3,13,14]

Recently, another group of TMCh, namely pentlandites (TM_9Ch_8), have also been considered to be extremely efficient catalysts. As bimetallic compounds ($Fe_{9-x}Ni_xS_8$, $Co_{9-y}Ni_yS_8$), pentlandites are characterized by excellent HER performances, as evidenced by the overpotential at the level of 280 mV (for a current density of 10 mA cm^{-2}), the Tafel slope of 72 mV dec^{-1}, and high stability under operating and corrosive conditions.[17–20] Furthermore, pentlandites can be used in bulk, rock-like geometries, ensuring high kinetic and efficiency with a highly conductive backbone, avoiding the same time-complicated synthesis process, and still reaching electrocatalytic properties at the level of nanostructured sulfides.[17] These outstanding properties of pentlandites are associated with very close intermetallic interactions and bimetallic bridges connected by sulfur anions. Active sites formed by the sulfur vacancies, in this case, are strongly favoured by H atoms, especially at 8c Wyckoff sites.[21] Some synergistic phenomena related to the co-existence of randomly distributed cations should also be mentioned.[22] It has been theoretically[14,23] and experimentally[14,24] proven that by combining two or more cations (particularly from the Co, Fe, and Ni subgroup), the respective d- and p-band shift, and states near the Fermi level overlap, increasing the metallic character and affecting the electrocatalytic activity by improving charge-transfer abilities, HER activity, and increasing the electrochemically active surface area. On this basis, the addition of Fe or Ni may significantly improve the activity of monometallic Co_9S_8,[14,20] while the Fe : Ni ratio in bimetallic pentlandites promotes changing the activity from HER to OER.[25] The anionic sublattice can also be modified by introducing Se anions.[26] An extremely interesting area of research that emphasizes these synergetic phenomena is the so-called high-entropy approach to materials design.[27] It was originally applied to metallic systems and since then, it has been translated into multiple types of other systems, including chalcogenides.[23,28–30] In our previous study on the possibility of obtaining high-entropy pentlandite $(Co, Fe, Ni)_9(S, Se)_8$, the potentially positive influence of multi-occupied sublattices on electrochemical activity was presented. It is well known that by tailoring the cationic composition in multimetallic compounds, significant changes in the electronic structure and electrocatalytic activity can be achieved mainly due to the shifting of the respective band centers, the occupancy of the bonding or antibonding orbitals, and bond covalencies.[14,24,29,31–33] A favorable effect on the material's electrical parameters is also possible, as demonstrated in our previous work.[23] On the other hand, similar effects may be reached by tailoring the anionic sublattices, a relatively new concept, untouched for the first high-entropy materials based on oxide compounds, and expanded for non-oxide materials.[23,26,29,30] Thus, the two possible approaches, namely tailoring the cationic (Co/Fe/Ni) ratio in 4-component (TM_9S_8) and 5-component ($TM_9S_4Se_4$), or tailoring the S/Se ratio in 5-component (TM_9Ch_8) pentlandites, should be considered as extremely promising methods aimed at improving their catalytic performances Although detailed studies on tailoring the Co/Fe/Ni in trimetallic pentlandites have already been described,[18] the effects of selenium concentration on the catalytic performance in 5-component pentlandites remain an open issue.

In this study, we present the electrocatalytic performance of 5-component, high-entropy pentlandites as a function of selenium concentration and sample processing, maintaining at the same time the concept of using bulk material and providing a simple and scalable synthesis procedure. The selenium solubility limit in trimetallic pentlandites, together with detailed structural characterization, has been examined for the first time. The sintering conditions and their influence on the sample morphology to obtain solid electrodes with optimal properties have also been investigated. Finally, we have determined the influence of the intrinsic material properties related to the S : Se substitution ratio, together with the densification level and the concentration of chalcogenide vacancies provided by the sintering conditions, on catalytic performance. This approach stands in opposition to current trends, imposing the need for additional processes, and involves maximizing the intrinsic properties of solid electrodes.

Experimental

High-purity elements in the form of powders (Co – 99.8% Alfa Aesar, Ni – 99.8% Alfa Aesar), granules (Fe – 99.98% Alfa Aesar), and the chalcogenides (S – 99.999% Alfa Aesar, Se – 99.999% Alfa Aesar) were weighed in the desired ratios, initially homogenized, and double sealed in quartz ampules (the smaller ampule inside the larger one) under vacuum conditions (10^{-3} atm). The material was synthesized from the as-prepared mixtures in a tube furnace by a two-step heat treatment. At first, the ampules were heated to 1000 °C (1 °C min^{-1}) and annealed for 24 h. In the second step, the temperature was decreased to 500 °C where the material was annealed for 72 h and then quenched by addition to the water. Electrochemical characteristics were performed for samples directly cut from ingots, or sintered pellets as a function of sintering temperature. In the latter case, the obtained ingots were milled into powder by using a manual agate mortar (providing a random distribution of grain sizes) or by a normalized processing procedure in a planetary mill (particle size at the level of 700–800 nm determined by Dynamic Light Scattering measurements). Subsequently, the powders were consolidated into disks with a diameter of 10 mm and height of about 3 mm by using the Inductive Hot Pressing (IHP) method and the following procedure: double rinsing with Ar (0.5 atm) at room temperature,

Table 1 Investigated pentlandite samples as a function of Se concentration together with nominal and real chemical compositions (corresponding directly to the samples that are discussed in the next sections)

Abbreviation	Nominal chemical composition	Estimated chemical composition
TM_9S_8	$Co_3Fe_3Ni_3S_8$	$Co_{3.13}Fe_{3.09}Ni_{3.09}S_{7.68}$
TM_9S_7Se	$Co_3Fe_3Ni_3S_7Se$	$Co_{3.11}Fe_{3.05}Ni_{3.13}S_{6.34}Se_{1.37}$
$TM_9S_6Se_2$	$Co_3Fe_3Ni_3S_6Se_2$	$Co_{3.08}Fe_{2.95}Ni_{2.96}S_{5.51}Se_{2.49}$
$TM_9S_5Se_3$	$Co_3Fe_3Ni_3S_5Se_3$	$Co_{2.94}Fe_{2.97}Ni_{2.97}S_{4.78}Se_{3.34}$
$TM_9S_4Se_4$	$Co_3Fe_3Ni_3S_4Se_4$	$Co_{3.01}Fe_{2.96}Ni_{2.92}S_{3.99}Se_{4.12}$
$TM_9S_3Se_5$	$Co_3Fe_3Ni_3S_3Se_5$	$Co_{2.97}Fe_{2.89}Ni_{2.92}S_{3.12}Se_{5.09}$
$TM_9S_2Se_6$	$Co_3Fe_3Ni_3S_2Se_6$	Multiphase
TM_9SSe_7	$Co_3Fe_3Ni_3SSe_7$	Multiphase
TM_9Se_8	$Co_3Fe_3Ni_3Se_8$	Multiphase

Table 2 Investigated pentlandite samples as a function of sintering temperature together with nominal and real chemical composition (corresponding directly to the samples that are discussed in the next sections)

Abbreviation	Sintering temperature [°C]	Nominal chemical composition	Estimated chemical composition
TM_9S_8_400	400	$Co_3Fe_3Ni_3S_8$	$Co_{3.13}Fe_{3.09}Ni_{3.09}S_{7.68}$
TM_9S_8_450	450	$Co_3Fe_3Ni_3S_8$	$Co_{3.21}Fe_{3.23}Ni_{3.21}S_{7.35}$
TM_9S_8_500	500	$Co_3Fe_3Ni_3S_8$	$Co_{3.38}Fe_{3.32}Ni_{3.36}S_{6.94}$

heating to 200 °C (100 °C min^{-1}), annealing for 5 min, heating to the final temperature (100 °C min^{-1}), annealing for 14 min under 50 MPa pressure and 1 min without pressure, cooling. The density of the sintered pellet was further examined with the use of Archimedes' principle and by volumetric measurements. Tables 1 and 2 show all investigated samples with nominal and real chemical compositions. The latter ones were determined based on the averaged element concentration provided by EDS analysis (actual results are presented in the next sections).

The phase compositions of the prepared samples (after synthesis and sintering process) were examined *via* X-ray diffraction (XRD) (apparatus: Empyrean PANanalytical apparatus (CuKα radiation)) and further analyzed using the X'Pert High Score Software. The microstructural observations and homogeneity of the samples were investigated by scanning electron microscopy combined with energy-dispersive X-ray spectroscopy (SEM + EDS) (apparatus: Thermoscientific Fischer Phenom XL scanning electron microscope equipped with EDS analyzer). The chemical state of elements was investigated by X-ray photoelectron spectroscopy (XPS) for chosen compositions. The measurements were conducted in a PHI VersaProbeII Scanning XPS system. The deconvolution of spectra was performed using the PHI MultiPak software (v.9.9.2).

Detailed information on the material structure was obtained by transmission electron microscopy (TEM) performed on a Tecnai TF 20 X-TWIN, FEI Company.

Electrochemical measurements were carried out using an electrochemical analyzer (MTM-ANKO) at room temperature. A conventional three-electrode system was used, with TM_3Ch_4 as the working electrode, Pt + Pt black acting as an auxiliary electrode, and Ag/AgCl (3 M KCl) as the reference electrode. The working electrode was made of polished (Al_2O_3-based polishing paste) sintered material or ingots without any additional processing, by connecting it directly to the Pt rod and placing it in a custom-made glass holder. The as-prepared electrode was sealed with silicone to ensure no contact between the electrolyte and the Pt rod and, at the same time, the surface of the pellet was in contact with the electrolyte without the involvement of lateral surfaces. Next, the electrodes were conditioned by several linear sweep voltammetric (LSV) cycles (200 mV s^{-1}, −400–400 mV measuring range) to achieve steady-state conditions and clear the surface from residual contamination. To avoid the overestimation of the obtained results, the electrochemical activity of the material was assessed based on the electrochemical active surface area (ECSA). The ECSA was determined based on electrochemical double-layer capacitance (C_{dl}) using cyclic voltammetry (CV), measured in the 0–300 mV range and with a 1.05–2000 mV s^{-1} scan rate. In this case, C_{dl} represents the linear regression of charging current densities as a function of scan rate, while ECSA provides the C_{dl} value divided by the specific capacitance of the samples of 0.035 mF cm^{-2}.[34] Notably, to compare the HER performance of the actual catalyst, overpotential values *vs.* RHE are usually given at a current density of 10 mA cm^{-2}. Due to the formation of the samples (solid electrodes), recorded current densities, and the occurrence of non-zero cathodic currents, the observed overpotential was determined with the application of more relevant current densities of 120 and 200 mA cm^{-2}.

Chronoamperometric measurements were performed for 30 h at a constant overpotential of 300 mV *versus* RHE. Electrochemical impedance spectroscopy (EIS) was recorded in the frequency range from 1 Hz to 50 kHz. In the model used to fit the experimental spectra, the circuit consisted of resistors, capacitors and a Warburg element. Based on the analysis of the impedance spectra, the charge-transfer resistance (R_{CT}) was evaluated. Chronoamperometry and EIS measurements were performed using a Gamry Interface 1010E apparatus.

Results and discussion

The selenium solubility limit in 5-component $TM_9S_{8-x}Se_x$ pentlandite (with an equimolar ratio of Co, Fe, and Ni) was determined as the first subject of this work. In Fig. 1 the cumulative XRD patterns of compounds from TM_9S_8 up to TM_9Se_8, together with fitting parameters and basic structural

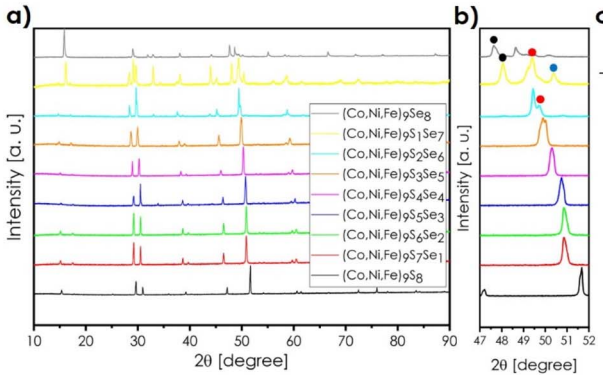

c)

Chemical composition	unit cel a=b=c [Å]	GoF	wRp
$(Co,Fe,Ni)_9Se_8$	mutliphase	6.86	8.77
$(Co,Fe,Ni)_9SSe_7$	multiphase	7.23	5.78
$(Co,Fe,Ni)_9S_2Se_6$	Multiphase	4.74	5.71
$(Co,Fe,Ni)_9S_3Se_5$	10.334 (± 0.0026)	5.68	6.61
$(Co,Fe,Ni)_9S_4Se_4$	10.235 (± 0.0019)	3.98	5.19
$(Co,Fe,Ni)_9S_5Se_3$	10.217 (± 0.0023)	2.50	4.63
$(Co,Fe,Ni)_9S_6Se_2$	10.150 (± 0.0016)	2.32	4.32
$(Co,Fe,Ni)_9S_7Se$	10.082 (± 0.0013)	2.05	4.22
$(Co,Fe,Ni)_9S_8$	10.008 (± 0.0008)	1.44	3.14

Fig. 1 (a) XRD diffraction pattern of $TM_9S_{8-x}Se_x$ samples; (b) the influence of Se concentration on the position of the most intense reflection $Q_v = 51.8$; (c) the unit cell together with fitting parameters; GoF – goodness of fit, w*R*p – weighted *R* profile.

data, are presented. Structural analysis indicated that selenium can substitute for sulfur sites in trimetallic pentlandite at a level of 63 molar%. Higher Se concentration (starting with (Co, Fe, Ni)$_9S_2Se_6$ composition) leads to multiphase systems with the pentlandite structure being the main phase with the addition of various selenides, such as FeSe (black dots in Fig. 1b), CoSe (red dots in Fig. 1b) and pyrite-like $TMCh_2$ structures (blue dots in Fig. 1b). This limited solubility of selenium suggests that the coexistence of all three metals (Co, Fe, and Ni) does not influence the Se : S substitution ratio as compared to bimetallic pentlandite as evidenced by similar solubility limits presented by Smialkowski *et al.*[26] In the solid solution range, an almost linear increase in lattice parameters with increasing Se concentration was observed (Fig. 1c), which was accompanied by a clear shift of analogous reflections towards lower angles, according to Vergard's rule (Fig. 1b).

As an example, the SEM micrograph of a cross-section of $TM_9S_3Se_5$ (with a critical Se concentration) together with the EDS analysis is presented in Fig. 2. SEM micrographs, together with EDS analysis of other single-phase compositions, are presented in the ESI† section (ESI Fig. 1–5). EDS analysis of all single-phase structures showed the high homogeneity of the materials, with the chemical composition being in accordance with the nominal ones. Furthermore, TEM investigation was performed for two extreme compositions, namely $Co_3Fe_3Ni_3S_8$ and $Co_3Fe_3Ni_3S_3Se_5$. It has been proven by selected area electron diffraction (SAED) studies that the pentlandite nanostructure is preserved in the volume of the grains. The EDS line scan across the selected grain revealed a chemical composition close to the nominal one with an equimolar Co : Fe : Ni ratio (ESI† Fig. 6).

XPS measurements performed for equimolar $Co_3Fe_3Ni_3S_4Se_4$ (ESI† Fig. 7) showed well-resolved peaks TM^{2+} $2p_{3/2}$, TM^{3+} $2p_{3/2}$,

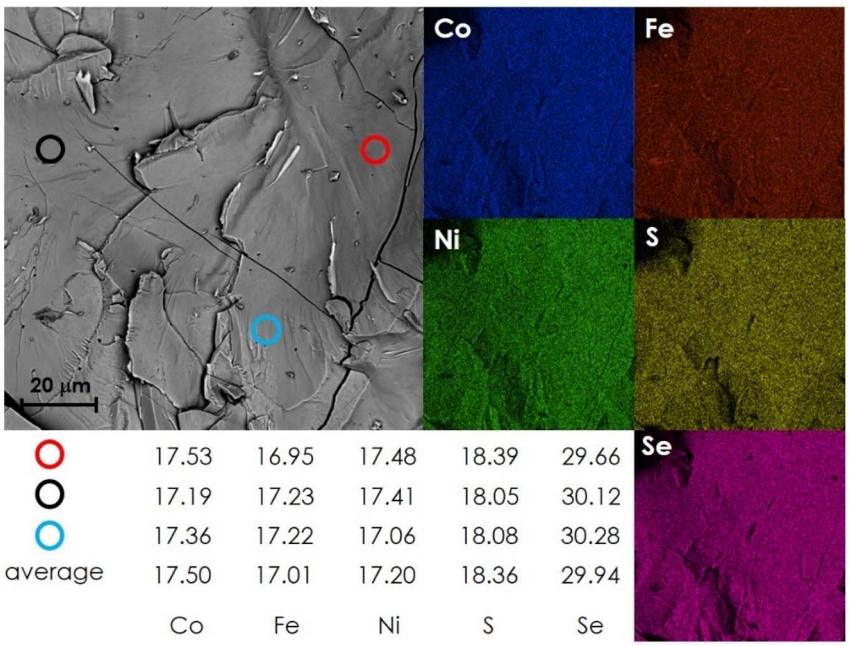

	Co	Fe	Ni	S	Se
○	17.53	16.95	17.48	18.39	29.66
○	17.19	17.23	17.41	18.05	30.12
○	17.36	17.22	17.06	18.08	30.28
average	17.50	17.01	17.20	18.36	29.94

Fig. 2 Cross-sectional SEM micrograph together with EDS point and map analysis (at%) for $TM_9S_3Se_5$ sample.

TM^{2+} $2p_{1/2}$, indicating the co-existence of TM cations in two different sites that differ in coordination number (octahedral and tetrahedral sites) in the material. The deconvoluted spectra indicated the presence of each TM mainly in the second oxidation state, typical for pentlandite-oriented studies.[17–19] For all TM, small amounts of metallic sites (at about 7, 16, and 2 molar% of total Co, Fe, and Ni content respectively) were also identified, as well as oxidized Co^{3+}/Fe^{3+} (23/44 molar%) cations, whose occurrence in tetrahedral sites (coordinated by S/Se at 8c Wyckoff sites) should positively influence catalytic activity.[21] The slightly shifted binding energies of TM towards higher values compared to mono- and bimetallic chalcogenides, as well as the position of the S 2p and Se 3d peaks, agree well with various non-stoichiometric chalcogenides, indicating the half-metallic character of the sample and the strong hybridization between TMs and Chs.[13,17,35]

In our previous study, the TM_9S_8 and TM_9S4Se_4 pentlandites were sintered utilizing Inductive Hot Pressing (IHP) and a final temperature of 400 °C was presented.[23] Since the previous work did not address the catalytic properties, here, the sintering procedure was repeated for all single-phase compositions and their electrochemical performances were tested. Since the densities of the materials pressed at 400 °C were not ideal and the thermal stability of the pentlandite phase was estimated up to 600 °C,[18] the sintering procedures were also performed for the final temperature set at 450 and 500 °C (above the boiling point of sulfur). Hot pressing is one of the basic techniques used to consolidate polycrystalline powder materials into highly densified solids and is widely used in thermoelectric, fuel cell or metallurgical processes.[36–40] In the field of electrocatalysis, where high surface development is usually desired, hot-pressing methods are not commonly used. Here, the term hot-pressing describes the process where the pressure is applied uniaxially at high temperatures. If the heat source is an induction furnace, the process is called inductive hot pressing. The simultaneous use of pressure and temperature allows a decrease in pressure and temperature compared to conventional pressing methods, and in turn, the maximum density can be achieved at relatively low temperatures, limiting grain size expansion at the same time.[40] For materials containing d-block elements, the densification process in this case is further assisted by the eddy currents present as a result of the induction coil. Ultimately, for materials with very high density and a large number of grain boundaries, alternative bulk structures, with favorable electrical properties, can be obtained. The XRD patterns and SEM micrographs of the TM_9S_8 are presented in Fig. 3, and ESI† Fig. 8, and 9, respectively, while the obtained densities are shown in ESI† Table 1. It has been found that sintering processes carried out at temperatures higher than 400 °C translate into the occurrence of a small area rich in Fe at the surface of the pellets (ESI† Fig. 8 and 9), most probably due to local reducing conditions (graphite dies), current flow across the material, and sulfur evaporation during the process. These Fe-rich areas constitute nonstoichiometric iron sulfide phases that are below XRD detection (a slightly broadened reflection at about 43.5 2θ can be indirectly related to small precipitation of the FeS phase) and can significantly affect electrochemical

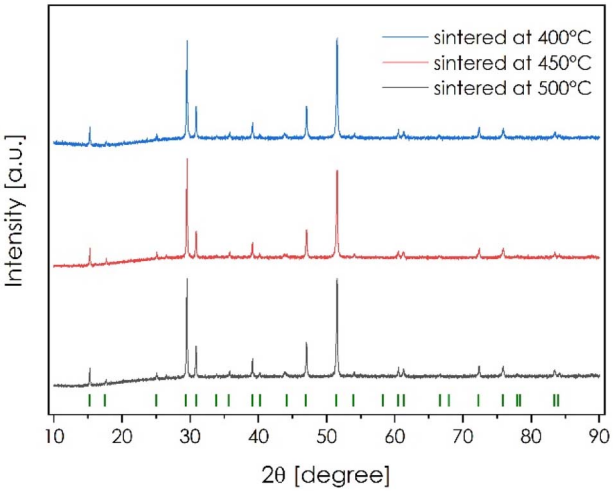

Fig. 3 XRD patterns of the TM_9S_8 pentlandite pellets sintered at 400, 450, and 500 °C.

properties, particularly when one considers the possible metal centers at the surface.[18] Although a clear relationship between the chemical composition, sintering temperature and final density of the materials can be observed (ESI† Table 1), it should also be noted that some level of Ch vacancies occurs on the surfaces of the sintered pellets, as evidenced by the decreased sulfur content (at 43 and 41 mol% for samples sintered at 450 and 500 °C, respectively, ESI† Fig. 8 and 9). Due to the increasing proportion of iron-rich inclusions on the surfaces and the relative densities close to 100%, the sintering processes were abandoned at temperatures greater than 500 °C. Finally, it seems obvious that the milling procedures, besides the strong influence on the material density, will also affect the catalytical performance. Thus, considering the catalytical activity of these solid materials, two different series of samples were considered: those sintered from powder obtained by hand-milled ingots, characterized by random particle size distribution, and those milled by a normalized procedure with a unimodal particle size distribution at the level of 700–800 nm.

Due to the customized design of each pentlandite electrode (available surface limited by the accuracy of siliconization processes at the edge of the material–glassy holder connections, the average geometric area ranges from 0.02 to 0.11 cm^2), the electrocatalytic performance was presented as a function of the electrochemical active surface area (ECSA) instead of the geometric (the electrocatalytic performance as a function of the geometric area is presented in ESI† Fig. 10). The ECSA of each sample, in turn, was determined based on cyclic voltammetry (CV, Fig. 4a) measurements performed in a wide range of scan speeds in the non-catalytic area. The linear regression of charging current densities provided by such CV measurements represents double-layer capacitance (C_{dl}, Fig. 4b) that is proportional to ECSA. For this reason, it is difficult to directly compare the performance of the obtained materials as a function of overpotential at a current density of −10 mA cm^{-2} [34], with the state-of the-the-art materials, since most of the literature data are presented as a function of the geometric area.

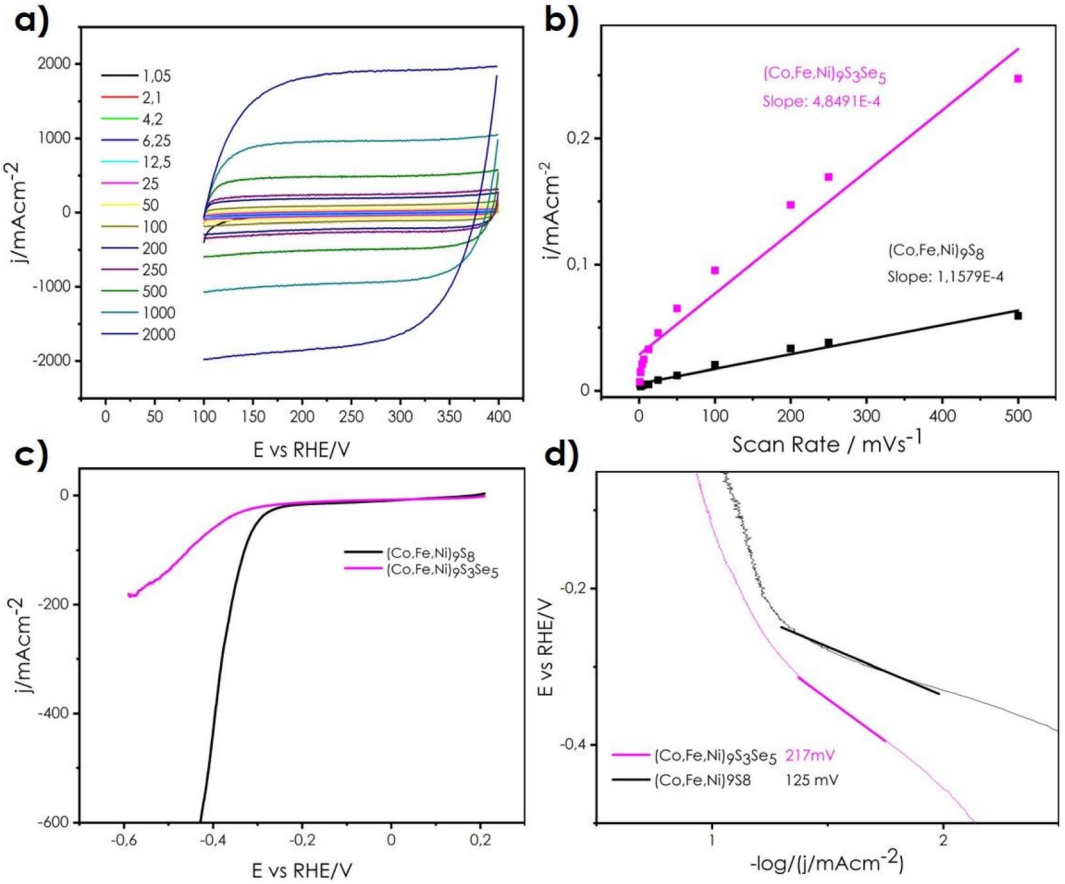

Fig. 4 (a) Cyclic voltammogram of the TM_9S_8 sample, (b) charging current density differences as a function of scan rate. The linear regression is equivalent to twice the double layer capacitance C_{dl} representing the ECSA, (c) linear sweep voltammograms (LSV) of the ingot samples normalized to the electrochemical surface area (ECSA) recorded at a sweep rate of 6.25 mV s^{-1} at 0.5 M H_2SO_4, (d) Tafel plots derived from voltammograms at a sweep rate 6.25 mV s^{-1} for the TM_9S_8 and $TM_9S_3Se_5$, respectively.

Since the HER performances of bimetallic and trimetallic pentlandites in acidic media are, also in rock-like geometry, already well described,[17,18,26] the presented results focus on the comparison of material performance as a function of Se concentration and morphology changes. To determine whether the sintering process has an impact on catalytic activity, we initially presented samples cut from ingots (directly from synthesis and without any further processing) as a benchmark. Here, the samples with extreme Se content (TM_9S_8 and $Tm_9S_3Se_5$) are presented (Fig. 4a–d). In the case of ingot samples, spontaneous crystal formation occurred without any nanostructured particles; thus, it should be stated that the final performance is related to the not-normalized surface roughness, random distribution of individual crystal facets (affecting catalytic performance[41]), as well as intrinsic properties of the materials, including the occupancy of individual cations in tetrahedral/octahedral sites, related vacancies in anionic sublattice, and synergistic effects (shifting respective bands near the Fermi level caused by multi-occupied sublattices).[42] The main role of catalytic activity in pentlandite-based systems is believed to be directly related to distances between the metal sites and related sulfur vacancy concentrations.[21] As with bimetallic selenium-rich pentlandites,[26] these distances and related intermetallic interactions increased with increasing Se concentration and therefore the HER activity also decreased. Table 3 presents overpotentials *versus* RHE at current densities equal to 50 and 150 mA cm^{-2}, in the ranges from 302/381 to 346/519 mV, respectively, and they decreased slightly after 2 h of electrolysis, indicating good HER performance. The non-zero cathode current for the samples with Se is quite remarkable. This unusual and recurring trend (increasing with the concentration of Se in all series of the samples) suggests the occurrence of some residual reactions involving S/Se anions on the surface of the material, charge compensation from the excessive number of Ch vacancies, or may be somehow connected to the non-ideal surface roughness and naturally (randomly) crystallized crystallographic planes. Based on the results presented in the next sections, these non-zero currents are related to the former phenomenon; thus, looking at the total envelope of the LSV curves (Fig. 4c), the selenium-rich material showed worse performance toward the HER. Also, the Tafel slope of the Se-rich ingot pentlandite (Fig. 4d) is high (217 mV dec^{-1}) and indicated a mixed Volmer–Heyrovsky reaction path, with the Volmer (proton adsorption) step being the limiting one, which confirms

Table 3 Basic electrocatalytic performance: overpotential *vs.* RHE as a function of current density and the calculated Tafel slopes of the ingot-like pentlandites

	Overpotential at 50 mA cm^{-2} [mV] *vs.* RHE		Overpotential at 150 mA cm^{-2} [mV] *vs.* RHE		Overpotential at 600 mA cm^{-2} [mV] *vs.* RHE		Tafel slope [mV dec^{-1}]	
Chemical composition	1st cyc.	After 2 h	1st cyc.	After 2 h	1st cyc.	After 2 h	1st cyc.	After 2 h
$Co_3Fe_3Ni_3S_8$	302	312	346	341	429	445	125	113
$Co_3Fe_3Ni_3S_3Se_5$	381	398	519	528	—	—	217	205

that the sulfur depletion in this material is somehow hindered, worsening at the same time the entire HER process. The Tafel slope of the trimetallic ingot with only sulfur anions (125 mV dec^{-1}) is at a level comparable to the one presented recently by Smialkowski *et al.*,[18] indicating a similar mechanism with an improved ratio of two absorbed protons (Tafel step) compared to the selenium-rich sample.

Surprisingly, the test measurements of the pellets sintered at 400 °C do not indicate a clear relationship between the HER performance and the chemical composition. Further attempts specified that in addition to the concentration of Se and the morphology of the samples, the density itself also strongly influences the catalytic activity of these solid electrodes. As can be seen in Fig. 5a, ingots that were milled in a hand-agate mortar (providing randomly distributed particle sizes) into powder and subsequently sintered under given conditions showed no clear tendency to be a function of chemical composition. Two of the best compositions were those with the highest Se concentration, which is an opposite effect to those presented for bimetallic compounds[26] and ingot electrodes (Fig. 4c). The TM_9S_8 sample was significantly better as compared to other single-phase materials (TM_9S_7Se, $TM_9S_6Se_2$, $TM_9S_5Se_3$), indicating a strong correlation between the performance of TM_9S_8 with the highest density in this series and the relatively small ECSA. Therefore, it could be concluded that porosity and related charge transfer abilities influence the HER performance at least as much as the intrinsic material properties. It also seems significant that the random distribution of grain sizes could also correlate with LSV curves as a function of the number of grain boundaries and the average grain size (although the results presented in the literature do not indicate special differences between bulk samples and nanosized samples, only for sulfur-rich samples[43,44]). Since any technological process should be standardized, samples with random grain size distribution are less important. To this end, another series of ingots was treated with a normalized grinding procedure to obtain a unimodal grain distribution of 700–800 nm (Fig. 5b). Taking into account the comparable and significantly higher level of densities (93% to 95%, ESI† Table 1), a clear relationship between the increase in Se concentration and the HER performance was observed, which is an opposite relationship to that of bimetallic systems[26] and the trimetallic composition presented in this work for ingot samples (Fig. 4).

Although the SEM/EDS analysis does not indicate any special changes in the chemical composition, it seems justified to conclude that when the density of the samples is close to the theoretical one, the sulfur vacancies are no longer the main reason for the high HER performance of solid pentlandites. It is well known that chalcogenides have a strong tendency to evaporate during any thermal treatment, especially in the presence of current flow.[45,46] When the longer and weaker TM–Se bonds compared to those of TM–S are taken into account, the concentration of Se vacancies will increase drastically with increasing Se concentration in the starting material, providing a higher number of TM-related active sites. Therefore, it seems that the sintering process of the Se-rich samples leads to high defect concentrations, followed by the creation of effective percolation paths. This can be indirectly confirmed by the

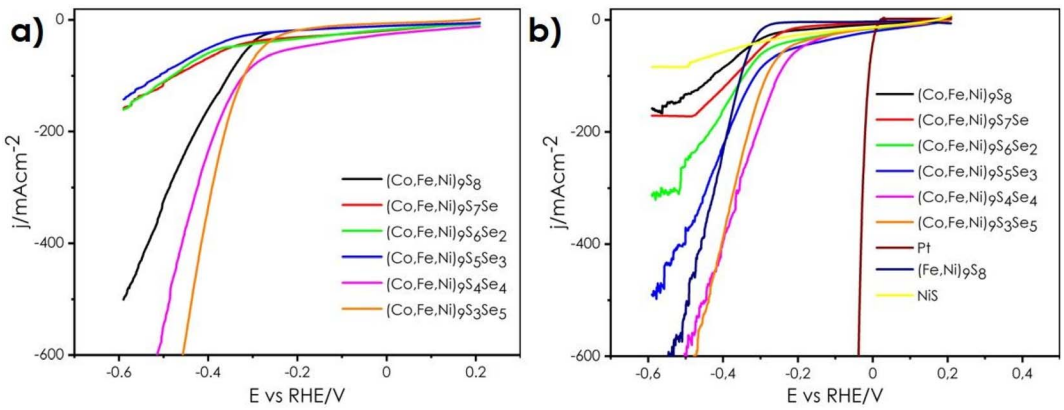

Fig. 5 LSV curves as a function of Se concentration normalized to the ECSA recorded at a sweep rate 6.25 mV s^{-1} at 0.5 M H_2SO_4: (a) pellets with random particle sizes, (b) pellets with normalized particle sizes.

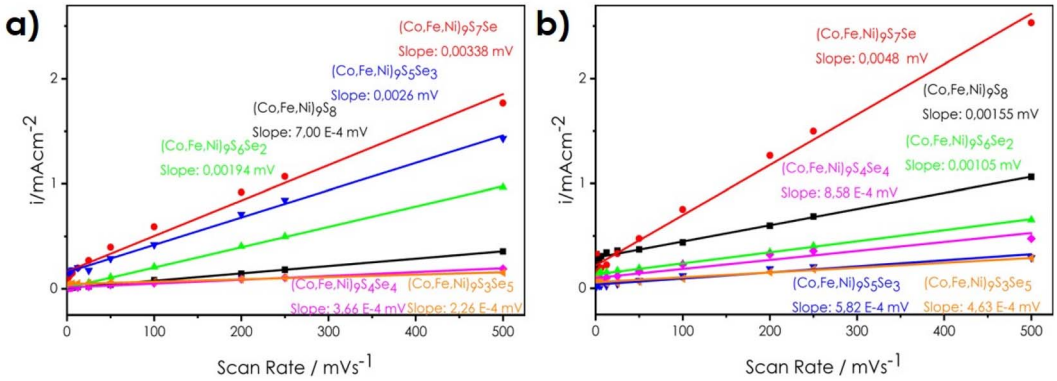

Fig. 6 Linear regression of the charging current density differences as a function of scan rate for pellets with random particle sizes (a) and pellets with normalized particle sizes (b).

presence of residual cathodic currents, the proportion of which increases with the selenium content. Thus, sintering with the IHP method, where eddy currents occur, leads to an inverse relation between HER activity and Se concentration in pentlandites. Notably, the electrochemically active area calculated by the analysis of the charging current density differences as a function of scan rate decreases with increasing Se concentration in both material series (Fig. 6), which indirectly translates into observed values in LSV curves. This trend coincides with the observation for the bimetallic seleno-analogues of pentlandites presented by Smialkowski,[26] where the decreasing ECSA for Se-rich samples were correlated with a limited ability to create defects on the sulfur sublattice. Thus, a general relationship started to become clear. The availability of the active surface and the intrinsic properties of pentlandites deteriorated with increasing Se content, which agrees well with the available data on bimetallic Se-rich pentlandites.[26] However, optimal sintering conditions provided very high density and related charge transfer abilities (charge transfer resistances R_{CT} for normalized sample series are presented in ESI† Fig. 11) together with a high concentration of Ch vacancies, which affected the improved catalytic performance, placing Se-rich pentlandites in a different light with reference to the bimetallic analogues.[26] The latter phenomenon strongly suggests that the thermal treatment of pentlandites is one of the key factors that lead to an inverse correlation as compared to the literature data. This is a typical disguising effect, the skillful optimization of which, based on materials science methods, can contribute to the deliberate improvement of the final properties. For comparison, the synthesis of the well-described bimetallic pentlandite ($Fe_{4.5}Ni_{4.5}S_8$) and nickel sulfide (NiS) was also performed. The pellets obtained under analogous conditions indicated that the multicomponent approach makes it possible to obtain materials whose reaction onset occurs at lower overpotentials in relation to the mono- or bimetallic systems. The overpotentials at certain current densities of $Fe_{4.5}Ni_{4.5}S_8$ were at a comparable level to the $Co_3Fe_3Ni_3S_5Se_3$ composition and significantly lower than the samples with higher Se contents. Due to the obtained current densities, non-zero cathodic currents, the relatively small active area (ECSA), and the presentation of the HER performance as a function of ECSA, it is difficult to directly compare these results with other literature data; however, in the ESI† section, recorded overpotentials at certain current densities of the normalized series are presented *versus* selected literature data (ESI† Table 3).

The determined Tafel slopes (Fig. 7a and b) showed a rather random distribution with a slight tendency to decrease with the increasing Se concentration. Here, these values are very high,

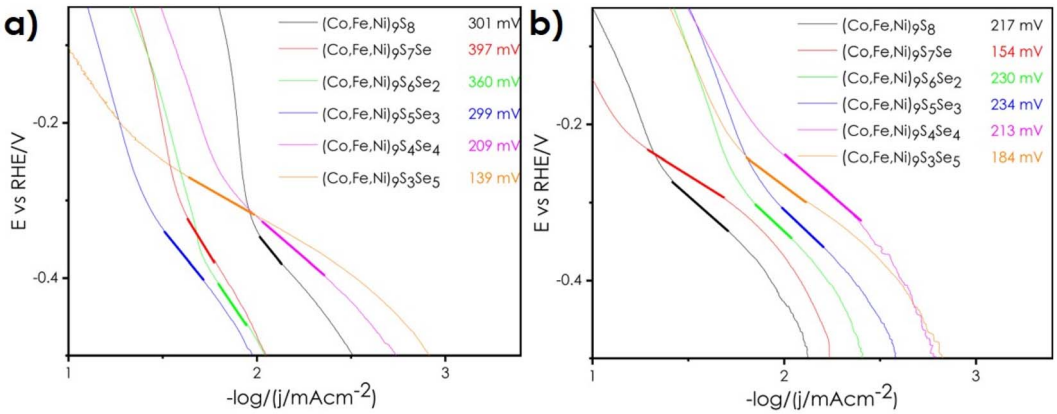

Fig. 7 Tafel slopes of pellets with random particle sizes (a) and pellets with normalized particle sizes (b).

Table 4 Basic electrocatalytic performance: overpotential *vs.* RHE as a function of current density and calculated Tafel slopes of the sintered pentlandites with normalized particle sizes

Chemical composition (particle size 700–800 nm)	Overpotential at 120 mA cm^{-2} [mV] *vs.* RHE		Overpotential at 200 mA cm^{-2} [mV] *vs.* RHE		Tafel slope [mV dec^{-1}]	
	1st cycle	After 2 h	1st cycle	After 2 h	1st cycle	After 2 h
$Co_3Fe_3Ni_3S_8$	460	452	Out of range	Out of range	217	188
$Co_3Fe_3Ni_3S_7Se$	398	444	Out of range	Out of range	154	156
$Co_3Fe_3Ni_3S_6Se_2$	363	404	436	481	230	157
$Co_3Fe_3Ni_3S_5Se_3$	333	393	385	466	234	207
$Co_3Fe_3Ni_3S_4Se_4$	264	269	309	307	213	159
$Co_3Fe_3Ni_3S_3Se_5$	296	321	333	362	184	164
$Fe_{4.5}Ni_{4.5}S_8$	360	345	389	377	68	71
NiS	Out of range	Out of range	Out of range	Out of range	618	585
Pt	13	19	21	24	56	56

indicating the Volmer–Heyrovsky mechanisms of H_2 evolution and the rather slow kinetics of the reaction. However, pellets obtained by normalized powders were characterized by significantly lower Tafel slope values, which should be connected by both the higher number of grain boundaries and the increased density, providing a fast charge-transfer ratio. As a summary of this section, Table 4 (and ESI† Tables 2 and 3) shows the overpotentials and Tafel slopes obtained during the first measurement and after 2 h of electrolysis. Surprisingly, after 2 h of operating conditions, the overpotentials increased slightly, suggesting that stabilization processes occur on the surfaces (charge equalization associated with defect concentration), or the surface area is blocked due to relatively low ECSA. The last effect should be connected to both the presence of Se in the anionic sublattice that blocks sulfur-depletion mechanisms responsible for hydrogen adsorption, as well as filling the preferred available vacancy sites (8c and 24d).[21,26] This seems particularly reasonable as one considers the slightly decreased or even improved overpotentials at certain current densities obtained for sulfur-rich compositions ($Co_3Fe_3Ni_3S_8$ and $Fe_{4.5}Ni_{4.5}S_8$, Table 4). A clear relation between the obtained overpotentials and densities of the samples was noticed here. On the other hand, after 2 h of electrolysis, the Tafel slopes decreased suggesting that the proton adsorption/desorption processes became more efficient with time. It should also be noted that the sample TM_9S_7Se that belongs to the normalized series deviates from general relationships, namely the decreasing Tafel slope as a function of Se concentration, indicating a strong dependence on ECSA (highest ECSA in the normalized series, Fig. 6b, ESI† Table 4).

The chronoamperometric curves for 2 hours of electrolysis at a constant potential of 300 mV *vs.* RHE, and SEM-EDS micrographs of the sample surfaces before and after the process are presented in the ESI† section (ESI† Fig. 12–18) to estimate the chemical stability of the materials. No significant changes were found in the morphology and chemical composition of the electrode surfaces, indicating good stability under operating conditions. To demonstrate long-term stability, the best-performing composition, namely $Co_3Fe_3Ni_3S_4Se_4$ was additionally tested over a period of 30 h of electrolysis (ESI† Fig. 19).

The results indicate that by applying bulk pentlandites with relatively low ECSA but easy and scalable synthesis procedures, it is possible to obtain materials whose intrinsic properties guarantee very high current densities per surface area. It has also been found that the density, ECSA, and defect concentration on the surfaces, provided by the sintering process, also strongly influence the HER performance (ESI† Table 4). Thus, the last part of this study focused on catalytic activity *versus* sintering temperature for the trimetallic samples without Se addition (due to strong Se evaporation during processes carried out at higher temperatures). The results presented in Fig. 8–10 and Tables 5 and 6 confirm the outstanding HER capabilities of pentlandites in this regard. It was found that current densities at a given overpotential can be drastically improved by applying higher temperature, which is related to the close to the theoretical density of the samples and very high defect

Table 5 Basic electrocatalytic performance: overpotential *vs.* RHE as a function of current density and calculated Tafel slopes of the sintered pentlandites with random particle sizes as a function of sintering temperature

TM_9S_8 (random particle size) sintering temp.	Overpotential at 120 mA cm^{-2} [mV] *vs.* RHE		Overpotential at 1000 mA cm^{-2} [mV] *vs.* RHE		Tafel slope [mV dec^{-1}]	
	1st cycle	After 2 h	1st cycle	After 2 h	1st cycle	After 2 h
400	369	397	428	457	268	264
450	283	294	307	319	105	96
500	243	241	263	280	90	95

Table 6 Basic electrocatalytic performance: overpotential *vs.* RHE as a function of current density and the calculated Tafel slopes of the sintered pentlandites with normalized particle sizes

TM_9S_8 (particle size 700–800 nm) sintering temp.	Overpotential at 120 mA cm^{-2} [mV] *vs.* RHE		Overpotential at 1000 mA cm^{-2} [mV] *vs.* RHE		Tafel slope [mV dec^{-1}]	
	1st cycle	After 2 h	1st cycle	After 2 h	1st cycle	After 2 h
400	460	452	Out of range	Out of range	209	178
450	348	455	369	502	77	109
500	374	571	411	Out of range	83	142

concentration. Referring to ESI† Fig. 8 and 9 (SEM micrographs) the average concentration of sulfur per area decreased from the level of 45 mol% to 43 mol% and finally 41 mol% for the pellets sintered at 450 and 500 °C, respectively. Therefore, both hand-milled and normalized powder series sintered at higher temperatures produced lower overpotentials at 120 mA cm^{-2} as compared to samples processed at 400 °C (Tables 5 and 6). Surprisingly, the hand-milled series provided better and more intuitive results, namely, increasing the HER efficiency (Fig. 8a) and decreasing the ECSA (Fig. 9a) along with increasing the temperature. The sample sintered at 500 °C was the best-performing material, characterized by a current density equal to 400 mA cm^{-2} at an overpotential of 300 mV, with a Tafel slope of 90 mV dec^{-1} (Fig. 10a). The remaining question was about the influence of the Fe-rich area on the sample surfaces (ESI† Fig. 8 and 9) on its catalytical activity. It seems that in addition to the density of the materials and the high defect concentration, we obtained a rather typical system: a conventional and randomly distributed precipitation of the active phase in the form of a nonstoichiometric iron sulfide anchored to the highly conductive and catalytically active surface in the form of pentlandite. The latter effect led to the appearance of unpredictable

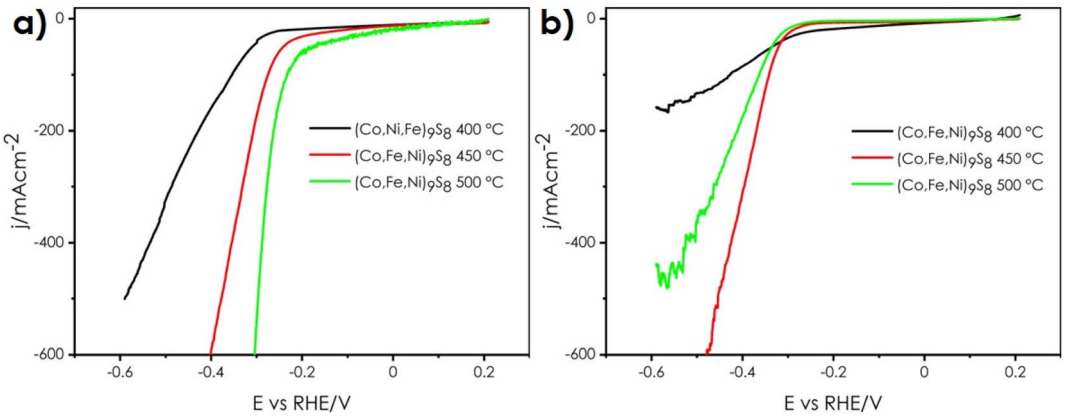

Fig. 8 LSV curves as a function of Se concentration normalized to ECSA, recorded at sweep rate 6.25 mV s^{-1} at 0.5 M H_2SO_4: (a) pellets with random particle sizes, (b) pellets with normalized particle sizes.

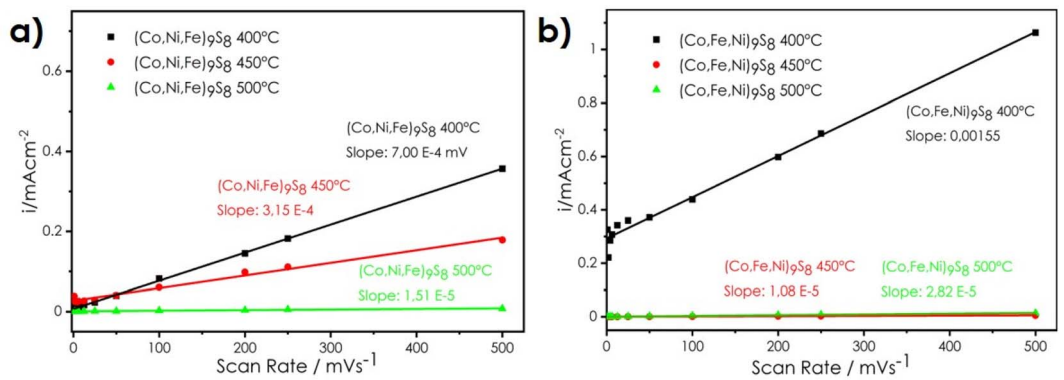

Fig. 9 Linear regression of the charging current density differences as a function of scan rate for pellets with random particle sizes (a) and pellets with normalized particle sizes (b).

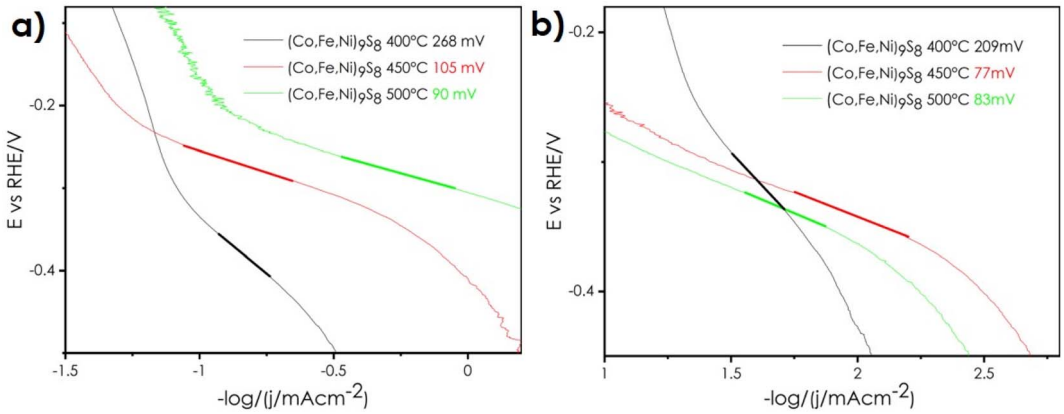

Fig. 10 Tafel slopes of pellets with random particle sizes (a) and pellets with normalized particle sizes (b).

synergistic phenomena, yielding solid electrodes with high efficiency. The positive influence of temperature treatment was also observable in the normalized series (Fig. 8b); however, the observed HER performance of the samples was significantly worsened as compared to the not-normalized ones. Furthermore, the sample sintered at 450 °C is better than the one sintered at 500 °C, suggesting that too much Fe-rich precipitation resulted in blocking the active surface (Fig. 9b and 10b) and limiting the positive influence of very high density. Therefore, it seems that once the material density is sufficiently high (by means of temperature or initial powder treatment), there is a certain optimal concentration of defects, in the form of other phase precipitations or vacancies in the anionic sublattice, which translates into the highest performance. Further studies should answer how to quantitatively estimate this optimal amount to develop the most favorable conditions.

Conclusions

In this work, the limit of the solubility of selenium in high-entropy pentlandites was determined at the level of 63 mol%. Single-phase compositions were sintered as a function of initial powder fineness and processing temperature. Multicomponent pentlandites were shown to achieve a high HER efficiency as solid electrodes, which may be translated into a simple application of this solution in the future. It has been found that the addition of Se worsens the intrinsic properties and reduces the active surface area of the materials. However, it seems that selenium has a stronger tendency to create vacancies during sintering processes conducted at 400 °C, followed by the formation of percolation paths. Thus, considering highly densified materials, it is possible to tailor and improve the performance of pentlandites by introducing Se as a precursor of a defect in the anionic sublattice without affecting the phase composition. It was also shown that the initial grain size of the powder, density, and defect concentration at the surfaces provided by temperature treatment allowed very high current densities to be achieved at relatively low overpotentials. Through the careful selection of the sintering conditions, a highly conductive material with active precipitations on the surface can be produced. Although the addition of Se makes such control difficult due to its too-strong tendency to evaporate, only S-rich samples should be considered at temperatures higher than 400 °C. These sulfur-rich pentlandites sintered at temperatures above the boiling point of sulfur involve a reduced sulfur content along with the precipitation of non-stoichiometric iron sulfides at the surface. Together with very high densities, solid pentlandite electrodes can achieve an overpotential of 240 mV at the current density of 120 mA cm^{-2}, with good stability, and reduced Tafel slopes at the level of 70–110 mV dec^{-1} (depending on initial grain size and final temperature). The proposed solution involving a combination of multicomponent materials together with optimization of the sintering process represents an unprecedented approach, allowing highly effective catalytic materials to be obtained through a relatively simple and productive preparation process.

Author contributions

Andrzej Mikuła: conceptualization, data curation, formal analysis, funding acquisition, investigation, methodology, project administration, resources, supervision, validation, visualisation, writing – original draft, writing – review & editing. Maciej Kubowicz: data curation, formal analysis, investigation, methodology, visualization, writing – review & editing. Julia Mazurków: investigation, formal analysis, methodology, visualization, writing – review & editing. Krzysztof Mars: investigation. Mathias Smialkowski: methodology, validation, formal analysis. Ulf-peter Apfel: supervision, formal analysis, validation, writing – review & editing. Marta Radecka: funding acquisition, project administration, resources, supervision, validation, writing – review & editing.

Conflicts of interest

There are no conflicts to declare.

Acknowledgements

Research project partly supported by program “Excellence initiative – research university” for the University of Science and

Technology, Poland. Ulf-Peter Apfel was funded by the Deutsche Forschungsgemeinschaft (DFG, German Research Foundation) under Germany's Excellence Strategy – EXC 2033 – 390677874 – RESOLV as well as APAP242/9–1, the Fraunhofer Internal Programs under grant no. Attract 097-602175. The authors are also thankful for support by the Mercator Research Center Ruhr (MERCUR.Exzellenz, 'DIMENSION' Ex-2021-0034 and 'Kata-Sign' Ko-2021-0016). This work was also funded in part by the National Science Centre, Poland, under grant no. 2022/45/B/ST8/03336.

Notes and references

1 N. Dubouis and A. Grimaud, *Chem. Sci.*, 2019, **10**, 9165–9181.
2 M. Ďurovič, J. Hnát and K. Bouzek, *J. Power Sources*, 2021, **493**, 229708.
3 M. E. Scofield, Y. Zhou, S. Yue, L. Wang, D. Su, X. Tong, M. B. Vukmirovic, R. R. Adzic and S. S. Wong, *ACS Catal.*, 2016, **6**, 3895–3908.
4 E. Fabbri, A. Habereder, K. Waltar, R. Kötz and T. J. Schmidt, *Catal. Sci. Technol.*, 2014, **4**, 3800–3821.
5 S. Anantharaj, S. R. Ede, K. Sakthikumar, K. Karthick, S. Mishra and S. Kundu, *ACS Catal.*, 2016, **6**, 8069–8097.
6 M. L. Tejaswini and K. P. Lakshmi, in *Proceedings of Second International Conference on Signal Processing, Image Processing and VLSI*, Research Publishing Services, Singapore, 2015, pp. 477–483.
7 R. Miao, B. Dutta, S. Sahoo, J. He, W. Zhong, S. A. Cetegen, T. Jiang, S. P. Alpay and S. L. Suib, *J. Am. Chem. Soc.*, 2017, **139**, 13604–13607.
8 J. S. Chen, J. Ren, M. Shalom, T. Fellinger and M. Antonietti, *ACS Appl. Mater. Interfaces*, 2016, **8**(8), 5509–5516.
9 F. Ma, Y. Liang, P. Zhou, F. Tong, Z. Wang, P. Wang, Y. Liu, Y. Dai, Z. Zheng and B. Huang, *Mater. Chem. Phys.*, 2020, **244**, 122642.
10 X. Geng, W. Sun, W. Wu, B. Chen, A. Al-Hilo, M. Benamara, H. Zhu, F. Watanabe, J. Cui and T. Chen, *Nat. Commun.*, 2016, **7**, 10672.
11 A. B. Laursen, S. Kegnæs, S. Dahl and I. Chorkendorff, *Energy Environ. Sci.*, 2012, **5**, 5577.
12 N. Jiang, Q. Tang, M. Sheng, B. You, D. Jiang and Y. Sun, *Catal. Sci. Technol.*, 2016, **6**, 1077–1084.
13 C. Zhou, H. Wu, F. Zhang and Y. Miao, *Crystals*, 2022, **12**, 666.
14 Y. Tang, H. Yang, J. Sun, M. Xia, W. Guo, L. Yu, J. Yan, J. Zheng, L. Chang and F. Gao, *Nanoscale*, 2018, **10**, 10459–10466.
15 W. Guo, Q. Van Le, H. H. Do, A. Hasani, M. Tekalgne, S.-R. Bae, T. H. Lee, H. W. Jang, S. H. Ahn and S. Y. Kim, *Appl. Sci.*, 2019, **9**, 5035.
16 N. T. Suen, S. F. Hung, Q. Quan, N. Zhang, Y. J. Xu and H. M. Chen, *Chem. Soc. Rev.*, 2017, **46**, 337–365.
17 B. Konkena, K. J. Puring, I. Sinev, S. Piontek, O. Khavryuchenko, J. P. Dürholt, R. Schmid, H. Tüysüz, M. Muhler, W. Schuhmann and U. P. Apfel, *Nat. Commun.*, 2016, **7**, 1–8.
18 M. Smialkowski, D. Siegmund, K. Stier, L. Hensgen, M. P. Checinski and U.-P. Apfel, *ACS Mater. Au*, 2022, **2**, 474–481.
19 S. Piontek, C. Andronescu, A. Zaichenko, B. Konkena, K. junge Puring, B. Marler, H. Antoni, I. Sinev, M. Muhler, D. Mollenhauer, B. Roldan Cuenya, W. Schuhmann and U.-P. Apfel, *ACS Catal.*, 2018, **8**, 987–996.
20 M. Smialkowski, D. Tetzlaff, L. Hensgen, D. Siegmund and U.-P. Apfel, *Chin. J. Catal.*, 2021, **42**, 1360–1369.
21 I. Zegkinoglou, A. Zendegani, I. Sinev, S. Kunze, H. Mistry, H. S. Jeon, J. Zhao, M. Y. Hu, E. E. Alp, S. Piontek, M. Smialkowski, U.-P. Apfel, F. Körmann, J. Neugebauer, T. Hickel and B. Roldan Cuenya, *J. Am. Chem. Soc.*, 2017, **139**, 14360–14363.
22 M. B. Z. Hegazy, K. Harrath, D. Tetzlaff, M. Smialkowski, D. Siegmund, J. Li, R. Cao and U.-P. Apfel, *iScience*, 2022, **25**, 105148.
23 A. Mikuła, J. Dąbrowa, A. Kusior, K. Mars, R. Lach and M. Kubowicz, *Dalton Trans.*, 2021, **50**, 9560–9573.
24 H. M. A. Amin, M. Attia, D. Tetzlaff and U. Apfel, *ChemElectroChem*, 2021, **8**, 3863–3874.
25 R. Subbaraman, D. Tripkovic, D. Strmcnik, K.-C. Chang, M. Uchimura, A. P. Paulikas, V. Stamenkovic and N. M. Markovic, *Science*, 2011, **334**, 1256–1260.
26 M. Smialkowski, D. Siegmund, K. Pellumbi, L. Hensgen, H. Antoni, M. Muhler and U. P. Apfel, *Chem. Commun.*, 2019, **55**, 8792–8795.
27 J.-W. Yeh, S.-K. Chen, S.-J. Lin, J.-Y. Gan, T.-S. Chin, T.-T. Shun, C.-H. Tsau and S.-Y. Chang, *Adv. Eng. Mater.*, 2004, **6**, 299–303.
28 Z. Deng, A. Olvera, J. Casamento, J. S. Lopez, L. Williams, R. Lu, G. Shi, P. F. P. Poudeu and E. Kioupakis, *Chem. Mater.*, 2020, **32**, 6070–6077.
29 L. Wu and J. P. Hofmann, *Curr. Opin. Electrochem.*, 2022, **34**, 101010.
30 M. W. Glasscott, *Curr. Opin. Electrochem.*, 2022, **34**, 100976.
31 J. Song, C. Wei, Z. F. Huang, C. Liu, L. Zeng, X. Wang and Z. J. Xu, *Chem. Soc. Rev.*, 2020, **49**, 2196–2214.
32 R. Jacobs, J. Hwang, Y. Shao-Horn and D. Morgan, *Chem. Mater.*, 2019, **31**, 785–797.
33 D. Tetzlaff, C. Simon, D. S. Achilleos, M. Smialkowski, K. Junge Puring, A. Bloesser, S. Piontek, H. Kasap, D. Siegmund, E. Reisner, R. Marschall and U. P. Apfel, *Faraday Discuss.*, 2019, **215**, 216–226.
34 C. C. L. McCrory, S. Jung, I. M. Ferrer, S. M. Chatman, J. C. Peters and T. F. Jaramillo, *J. Am. Chem. Soc.*, 2015, **137**, 4347–4357.
35 S. Ganguli, S. Ghosh, G. Tudu, H. V. S. R. M. Koppisetti and V. Mahalingam, *Inorg. Chem.*, 2021, **60**, 9542–9551.
36 J. M. Torralba, in *Comprehensive Materials Processing*, Elsevier, 2014, pp. 281–294.
37 P. Nieroda, J. Leszczyński, A. Mikuła, K. Mars, M. J. Kruszewski and A. Koleżyński, *Ceram. Int.*, 2020, **46**, 25460–25466.
38 P. Nieroda, A. Kusior, J. Leszczyński, P. Rutkowski and A. Koleżyński, *Materials*, 2021, **14**, 3650.

39 A. Zhou, in *Advances in Science and Technology of Mn+1AXn Phases*, Elsevier, 2012, pp. 21–46.
40 J. Zhang, H. Zhang, J. Wu and J. Zhang, in *Pem Fuel Cell Testing and Diagnosis*, Elsevier, 2013, pp. 43–80.
41 L. Lu, S. Yu and H. Tian, *J. Colloid Interface Sci.*, 2022, **607**, 645–654.
42 D. Siegmund, N. Blanc, M. Smialkowski, K. Tschulik and U. Apfel, *ChemElectroChem*, 2020, **7**, 1514–1527.
43 C. L. Bentley, C. Andronescu, M. Smialkowski, M. Kang, T. Tarnev, B. Marler, P. R. Unwin, U.-P. Apfel and W. Schuhmann, *Angew. Chem., Int. Ed.*, 2018, **57**, 4093–4097.
44 D. Siegmund, N. Blanc, M. Smialkowski, K. Tschulik and U. Apfel, *ChemElectroChem*, 2020, **7**, 1514–1527.
45 D. R. Brown, T. Day, T. Caillat and G. J. Snyder, *J. Electron. Mater.*, 2013, **42**, 2014–2019.
46 P. Qiu, X. Shi and L. Chen, *Energy Storage Mater.*, 2016, **3**, 85–97.